JGR Space Physics

RESEARCH ARTICLE
10.1029/2019JA027422

Special Section:
Particle Dynamics in the Earth's Radiation Belts

The Effect of Plasma Boundaries on the Dynamic Evolution of Relativistic Radiation Belt Electrons

Dedong Wang[1], Yuri Y. Shprits[1,2,3], Irina S. Zhelavskaya[1,2], Frederic Effenberger[1], Angelica M. Castillo[1,2], Alexander Y. Drozdov[3], Nikita A. Aseev[1,2], and Sebastian Cervantes[1,2]

[1]GFZ German Research Centre for Geosciences, Potsdam, Germany, [2]Institute of Physics and Astronomy, University of Potsdam, Potsdam, Germany, [3]Department of Earth, Planetary, and Space Sciences, University of California, Los Angeles, CA, USA

Abstract Understanding the dynamic evolution of relativistic electrons in the Earth's radiation belts during both storm and nonstorm times is a challenging task. The U.S. National Science Foundation's Geospace Environment Modeling (GEM) focus group "Quantitative Assessment of Radiation Belt Modeling" has selected two storm time and two nonstorm time events that occurred during the second year of the Van Allen Probes mission for in-depth study. Here, we perform simulations for these GEM challenge events using the 3D Versatile Electron Radiation Belt code. We set up the outer L^* boundary using data from the Geostationary Operational Environmental Satellites and validate the simulation results against satellite observations from both the Geostationary Operational Environmental Satellites and Van Allen Probe missions for 0.9-MeV electrons. Our results show that the position of the plasmapause plays a significant role in the dynamic evolution of relativistic electrons. The magnetopause shadowing effect is included by using last closed drift shell, and it is shown to significantly contribute to the dropouts of relativistic electrons at high L^*. We perform simulations using four different empirical radial diffusion coefficient models for the GEM challenge events, and the results show that these simulations reproduce the general dynamic evolution of relativistic radiation belt electrons. However, in the events shown here, simulations using the radial diffusion coefficients from Brautigam and Albert (2000) produce the best agreement with satellite observations.

Key Points:
- We investigate the effect of different plasmapause positions and radial diffusion coefficients during the four GEM challenge events
- Including the magnetopause shadowing effect by using the last closed drift shell helps to reproduce the dropouts
- The three-dimensional Versatile Electron Radiation Belt code reproduces the general dynamics of relativistic electrons during GEM challenge events

Supporting Information:
- Supporting Information S1

Correspondence to:
D. Wang,
dedong@gfz-potsdam.de

Citation:
Wang, D., Shprits, Y. Y., Zhelavskaya, I. S., Effenberger, F., Castillo, A., Drozdov, A. Y., et al. (2020). The effect of plasma boundaries on the dynamic evolution of relativistic radiation belt electrons. *Journal of Geophysical Research: Space Physics*, *125*, e2019JA027422. https://doi.org/10.1029/2019JA027422

Received 19 SEP 2019
Accepted 20 MAR 2020
Accepted article online 23 APR 2020

1. Introduction

Understanding the dynamic evolution of relativistic electrons in the Earth's radiation belts under different geomagnetic conditions is challenging, due to the delicate balance between various acceleration and loss processes. Different adiabatic and nonadiabatic processes have been proposed to cause the acceleration and loss of relativistic electrons (e.g., Millan & Baker, 2012; Shprits, Elkington, et al., 2008; Shprits, Subbotin, et al., 2008; Thorne, 2010). Adiabatic variations occur when the forces acting on particles remain virtually unchanged on the time and spatial scale associated with the adiabatic invariant (e.g., Roederer, 1970; Schulz & Lanzerotti, 1974). During geomagnetic storms, the slow enhancement of the ring current causes the expansion of magnetic field lines in the inner magnetosphere inside the peak of the ring current. To conserve the third invariant, electrons move outward. Meanwhile, the first and second invariant are also conserved. This process causes electrons to lose energy and is referred to as the Dst effect (Kim & Chan, 1997). During this process, fixed energy channels of instruments on board satellites observe a decrease of fluxes. Adiabatic changes are reversible, and the flux of electrons with a certain energy can be recovered after the storm. In addition to adiabatic variations, there are also nonadiabatic changes. Several nonadiabatic processes are proposed to account for loss and acceleration of the radiation belt electrons. There are various plasma waves with frequencies comparable to the frequencies associated with the adiabatic motions (e.g., Roederer, 1970; Schulz & Lanzerotti, 1974). These waves can violate the adiabatic invariant and cause nonadiabatic changes of particles. For example, ultralow frequency (ULF) waves oscillate with a similar frequency to the timescale of the drift motion of relativistic electrons. Therefore, ULF waves can violate the third adiabatic invariant of particles, thus driving inward or outward radial diffusion and causing acceleration or deceleration (e.g., Fälthammar, 1965; Fu et al., 2011; Lyons & Thorne, 1973; Ozeke et al., 2014; Shprits

& Thorne, 2004). Coupled with the magnetopause shadowing effect, which generates a sharp gradient near the boundary, ULF waves can drive particle motion outward and finally result in loss to the magnetopause (e.g., Mann et al., 2016; Shprits et al., 2006; Tu, Xiang, et al., 2019; Yu et al., 2013; Turner et al., 2012). Electromagnetic ion cyclotron (EMIC) waves are suggested to cause fast loss of radiation belt electrons (Thorne & Kennel, 1971). The minimum resonance energies of electrons which can be significantly influenced by EMIC waves are higher than 2 MeV in most cases (e.g., Cao et al., 2017; Chen et al., 2019; Drozdov et al., 2017; Ni et al., 2018; Shprits et al., 2013, 2016). Very low frequency (VLF) waves oscillate at frequencies similar to the frequencies of the gyration and bounce motion of particles. Thus, VLF waves can cause local diffusion in pitch angle and energy, which may lead to the precipitation or enhancement of radiation belt electrons (e.g., Horne & Thorne, 1998, 2003). For example, outside the plasmasphere, chorus waves are believed to play an important dual role in both the enhancement and precipitation of electrons (e.g., Thorne, 2010). Inside the plasmasphere, plasmaspheric hiss waves can cause the slow decay of radiation belt electrons with loss time scales on the order of 5 to 10 days (e.g., Lyons et al., 1972; Orlova et al., 2014). In general, the plasmapause separates chorus waves outside the plasmasphere and hiss waves inside the plasmasphere.

"To concentrate community efforts and maximize scientific returns," the U.S. National Science Foundation's Geospace Environment Modeling (GEM) focus group "Quantitative Assessment of Radiation Belt Modeling (QARBM)" has selected two storm time and two nonstorm time challenge events that occurred during the second year of the Van Allen Probes mission for in-depth study (Tu, Li, et al., 2019). A number of studies have been performed for these GEM challenge events (Tu, Li, et al., 2019 and references therein). In particular, the storm time enhancement event on 17 March 2013 has been extensively studied using methods of both observations (e.g., Baker et al., 2014; Boyd et al., 2014; Foster et al., 2017, 2014; Olifer et al., 2018) and simulations, including Fokker-Planck, magnetohydrodynamics, and test particle simulations, based on both quasi-linear and nonlinear theories (e.g., Aseev et al., 2019; Hudson et al., 2015; Kubota & Omura, 2018; Li et al., 2014; Ma et al., 2018; Shprits et al., 2015; Xiao et al., 2014; Wang et al., 2017). These studies suggest that chorus waves play a crucial role in the enhancement of radiation belt electrons during this event. For example, by exploring the phase space density (PSD) profile of electrons at different energies, Boyd et al. (2014) suggest that, during this event, electrons with first adiabatic invariant, μ, lower than 200 MeV/G (approximately 200 keV and 50° pitch angle at $L^* = 6.6$) have a source in the plasmasheet. After their injection and radial diffusion into the inner magnetosphere, it is very likely that they are accelerated by chorus waves to higher μ. Xiao et al. (2014) performed 2D simulations to check the effect of intensified chorus waves observed by the Van Allen Probes, and they found that those chorus waves account for the enhancement of relativistic electrons at $L = 4.5$. By performing 2D simulations using a chorus wave distribution inferred from low-altitude satellite measurements, Li et al. (2014) showed that chorus-driven acceleration can explain the observed peak in the electron PSD at $L = 4.25$. By using a 3D code, Wang et al. (2017) supported the scenario that after injection and radial diffusion, seed populations are accelerated by chorus waves. By performing Versatile Electron Radiation Belt 4D (VERB-4D) simulations, which combine convective and diffusive processes, Shprits et al. (2015) reproduced the enhancement of electrons at energies of 0.2, 0.4, 0.7, and 1 MeV for the storm on 17 March 2013.

The storm time dropout event on 1 June 2013 has been studied by Kang et al. (2018) using the Comprehensive Inner Magnetosphere-Ionosphere model. They suggested that the magnetopause shadowing effect and the outward radial diffusion resulted in the flux dropout of energetic electrons. The effects of chorus waves and hiss waves are not included in their work. For the nonstorm time dropout event on 24 September 2013, Su et al. (2016) performed 3D simulations and suggested that this dropout is mainly caused by wave-induced precipitation by plasmaspheric hiss waves and EMIC waves. For the nonstorm time enhancement event on 19 September 2013, Ma et al. (2018) conducted 3D simulations for 2 days (19 and 20 September 2013). Their results show that the incorporation of both radial diffusion and local diffusion reasonably reproduces the observed location and magnitude of electron flux enhancements. By comparing the effects of local acceleration by chorus waves and radial diffusion driven by ULF waves, Ma et al. (2018) suggested that radial diffusion by ULF waves play a dominant role in this enhancement event within the Van Allen Probe orbits ($L < 6$). In their study, they used Van Allen Probes' observations to set up the initial conditions, lower ($L = 2.5$) and upper ($L = 6$) L-shell boundaries, which are very close to the region where the enhancement occurs ($5 \leq L \leq 6$). They also used Van Allen Probe measurements to update the lower and upper energy boundaries, which are from 104 keV to 5.23 MeV at $L = 6$ and from 300 keV to 10 MeV at $L = 4$. These boundaries are close to the energy and L range where enhancements of electron flux are observed during

the nonstorm event, and as a result, the data-driven boundaries may be a contributing factor. In addition, event-specific wave distributions inferred from low-altitude satellites measurements are also adopted in their study.

In the present study, we extend previous works on these GEM challenge events by performing simulations using the VERB-3D code to investigate the effects of the plasmapause and magnetopause locations on the dynamic evolution of relativistic electrons in the outer radiation belt. Our current study differs from the aforementioned simulation papers about these GEM challenge events in the following aspects:

- None of these previous studies investigated the four events in a single paper. Here, we systematically perform 3D simulations for these events.
- None of the previous studies performed simulations to investigate the effect of magnetopause shadowing using the last closed drift shell for all these events. It is noteworthy that during the review process of the current paper, a 1D simulation study using a radial diffusion model was published recently by Ozeke et al. (2020). They assessed the effects of the magnetopause shadowing effect and radial diffusion on the loss and recovery of ultrarelativistic (>2 MeV) electrons during "electron extinction" events in March 2013 and 2015. Our current paper focuses on the dynamic evolution of relativistic electrons at an energy of 0.9 MeV. Thus, it is not straightforward to compare our results with the results from Ozeke et al. (2020) for the storm event on 17 March 2013. In addition, the lifetime parameterization that they used for ultrarelativistic (>2 MeV) electrons outside the plasmapause (Gu et al., 2012) were developed for the electrons with energy lower than 2 MeV, which results in uncertainties for their study.
- None of the previous studies investigated the effect of the plasmapause position on the dynamic evolution of relativistic electrons.
- Most of these previous modeling studies of the GEM challenge events set up boundary conditions using Van Allen Probe data that are very close to the energies and L-shells of interest. Such an introduction of Van Allen Probe data at the lower and upper energy boundary conditions, initial conditions, lower and higher L-shell boundary conditions may affect the simulation results and may make it difficult to distinguish the results of the physics-based modeling from the simple propagation of satellite data from the boundary conditions. In our current study, instead of using Van Allen Probe measurements to set up the upper L boundary condition at $L = 5.5$, we use measurements from the Geostationary Operational Environmental Satellites (GOES) at geostationary orbit (GEO), which is the only data-driven boundary condition in our simulations. In this way, we analyze the results of the simulations in the regions sufficiently far away from any data-driven boundary condition. Extending the outer boundary condition to a region further from the Earth can lead to a better understanding of the effect of the competing processes, especially between radial and local diffusion. It can be also helpful to determine which mechanism is dominant and to objectively judge the performance of the modeling codes.
- Most of these previous simulation studies for the GEM challenge events used event-specific wave data, either taken from Van Allen Probe in situ observation or inferred from low Earth orbit (LEO) satellites. In situ wave measurements from the Van Allen Probes cannot provide the global distribution of waves in each event. The wave distribution inferred from LEO satellites such as the Polar Orbiting Environmental Satellites (POES) can provide global wave parameters (Chen et al., 2014; Li et al., 2013; Ni et al., 2014). This technique has been validated in several event studies (e.g., Ma et al., 2018; Thorne et al., 2013; Tu et al., 2014) and needs further testing using accumulated data sets of conjugate observations of waves and precipitation. In particular, due to the finite field of view of the instrument, it is not easy to distinguish precipitated particles from trapped particles. Even a small fraction of the trapped population inside the field of view of the instrument can significantly affect the analysis of the precipitation. Moreover, geographic changes in the magnetic field at LEO may introduce additional uncertainties. As models often consider only the ratio of 0° to 90° detector measurements, such a ratio may appear to not always be representative of the wave activity. In this study, instead of using event-specific waves, we use empirical wave models.

Our paper is organized as follows: first, we describe the VERB-3D code and the parameters adopted for our numerical simulations in section 2. Then in section 3, we present simulation results and their validation against satellite observations. Results and other possible mechanisms are discussed in section 4. Finally, we summarize our findings and outline directions for future studies in section 5.

2. Model Description

The dynamic evolution of electrons in the radiation belts can be described by the bounce- and magnetic local time (MLT)-averaged Fokker-Planck equation (e.g., Schulz & Lanzerotti, 1974; Shprits et al., 2009):

$$\frac{\partial f}{\partial t} = L^{*2}\frac{\partial}{\partial L^*}\Big|_{\mu,J}\left(\frac{1}{L^{*2}}D_{L^*L^*}\frac{\partial f}{\partial L^*}\Big|_{\mu,J}\right) + \frac{1}{p^2}\frac{\partial}{\partial p}\Big|_{\alpha_0,L^*} p^2\left(D_{pp}\frac{\partial f}{\partial p}\Big|_{\alpha_0,L^*} + D_{p\alpha_0}\frac{\partial f}{\partial \alpha_0}\Big|_{p,L^*}\right) + \frac{1}{T(\alpha_0)\sin(2\alpha_0)}\frac{\partial}{\partial \alpha_0}\Big|_{p,L^*} T(\alpha_0)\sin(2\alpha_0)\left(D_{\alpha_0\alpha_0}\frac{\partial f}{\partial \alpha_0}\Big|_{p,L^*} + D_{\alpha_0 p}\frac{\partial f}{\partial p}\Big|_{\alpha_0,L^*}\right) - \frac{f}{\tau_{lc}}, \quad (1)$$

where f is the electron PSD; t is time; μ and J are the first and second adiabatic invariant; L^* is inversely proportional to the third adiabatic invariant; p is the relativistic momentum of electrons; α_0 is the equatorial pitch angle of particles; $T(\alpha_0)$ is a function related to the bounce frequency and can be approximated as (Lenchek & Singer, 1962)

$$T(\alpha_0) = 1.3802 - 0.3198(\sin\alpha_0 + \sin^{1/2}\alpha_0); \quad (2)$$

and D_{LL}, D_{pp}, $D_{p\alpha_0}$, $D_{\alpha_0 p}$, and $D_{\alpha_0\alpha_0}$ in equation (1) are the bounce- and MLT- averaged scattering rates (or diffusion coefficients) due to resonant wave-particle interactions. τ_{lc} in equation (1) is the lifetime parameter accounting for losses of particles inside the loss cone due to collisions with atmospheric neutrals. In this study, the lifetime τ_{lc} is set to a quarter of a bounce period for electrons inside the loss cone and to infinity outside the loss cone.

2.1. Radial Diffusion Coefficients

The radial diffusion coefficient due to interactions with ULF waves is adopted from Brautigam and Albert (2000):

$$D_{LL}(\mathrm{Kp}, L) = 10^{0.506\mathrm{Kp}-9.325}L^{10},\ [1/\mathrm{day}], \quad (3)$$

where the parameter L refers to L^*. This radial diffusion model is based on a simple fit of the ground measurements at $L = 4$ (Lanzerotti & Morgan, 1973) and in situ geosynchronous measurements at $L = 6.6$ (Lanzerotti et al., 1978). Brautigam and Albert (2000) followed the expressions for D_{LL}^M proportional to L^{10} derived by Fälthammar (1965). However, it is noteworthy that the slope of the line connecting the two data points is steeper at low Kp and levels off at high Kp compared with L^{10}, as can be seen in the Figure 5 of Brautigam and Albert (2000). In addition, this parameterization is valid for Kp $\leq$ 6. In this study, however, we extrapolate it also to larger Kp values. In the events studied here the maximum Kp is 7.

In recent years, several other radial diffusion coefficient models were developed using the formula derived by Fei et al. (2006). For example, using ground magnetometer data and in situ measurements, Ozeke et al. (2014) developed analytic expressions for radial diffusion coefficients. In their model, the total radial diffusion coefficient was separated into two terms; one term due to the azimuthal electric field:

$$D_{LL}^E(\mathrm{Kp}, L) = 2.16\times10^{-8}L^6 10^{0.217L+0.461\mathrm{Kp}},\ [1/\mathrm{day}], \quad (4)$$

and the other term due to the compressional magnetic field component of the ULF waves:

$$D_{LL}^B(\mathrm{Kp}, L) = 6.62\times10^{-13}L^8 10^{-0.0327L^2+0.625L-0.0108\mathrm{Kp}^2+0.499\mathrm{Kp}},\ [1/\mathrm{day}]. \quad (5)$$

In this study, we also perform VERB-3D simulations using the total radial diffusion coefficients from Ozeke et al. (2014). In addition, using 7 years of data from the Time History of Events and Macroscale Interactions during Substorms satellites, Liu et al. (2016) derived an empirical expression of the radial diffusion coefficients due to the electric field as a function of L, Kp, and the first adiabatic invariant μ of the electrons:

$$D_{LL}^E(\mathrm{Kp}, L, \mu) = 1.115\times10^{-6}L^{8.184}10^{0.281\mathrm{Kp}}\mu^{-0.608},\ [1/\mathrm{day}]. \quad (6)$$

Based on the discussion in Liu et al. (2016) about applicability of their model, we set the radial diffusion coefficients for electrons below 400 MeV/G equal to those radial diffusion coefficients at $\mu = 400$ MeV/G. In addition, using 3 years of Van Allen Probe data, Ali et al. (2016) obtained the radial diffusion coefficients due to the ULF wave power in the compressional component of the magnetic field:

$$D_{LL}^B(\mathrm{Kp}, L) = \exp(-16.253 + 0.224\mathrm{Kp}L + L),\ [1/\mathrm{day}], \quad (7)$$

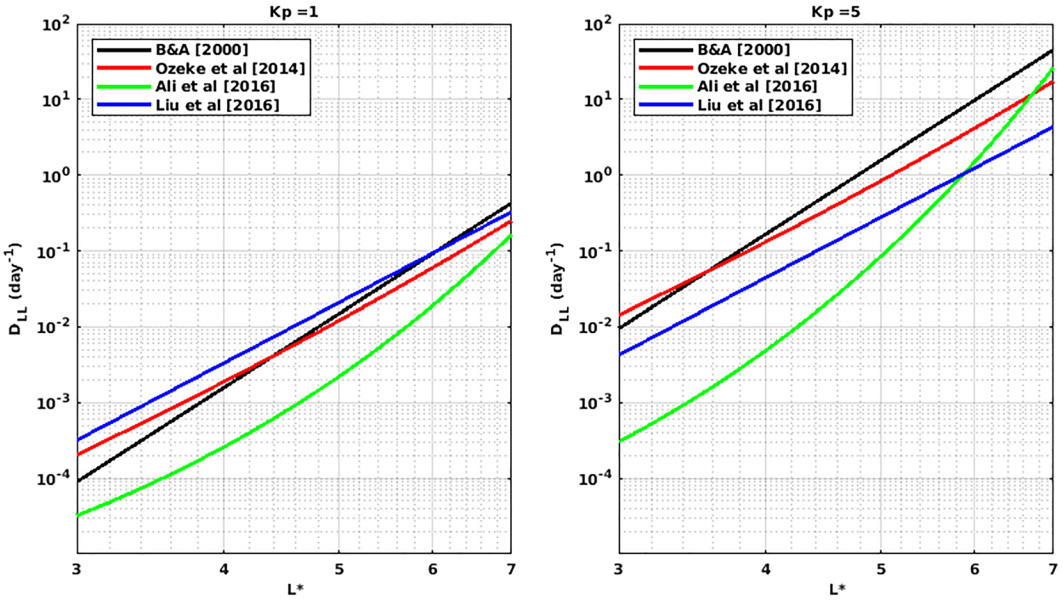

Figure 1. Different radial diffusion coefficients as a function of L^* at Kp = 1 and Kp = 5. The black, red, green, and blue lines show the radial diffusion coefficients calculated following Brautigam and Albert (2000), Ozeke et al. (2014), Ali et al. (2016), and Liu et al. (2016) (for a fixed value of μ = 700 MeV/G), respectively.

and the radial diffusion coefficients due to the azimuthal component of the electric field:

$$D_{LL}^{E}(\mathrm{Kp}, L) = \exp(-16.951 + 0.181\mathrm{Kp}L + 1.982L),\ [1/\mathrm{day}]. \quad (8)$$

They also stated that most of the time the magnetic component contributes very little and the total radial diffusion is mainly due to the electric component of the ULF waves. In this study, we also perform simulations using the total radial diffusion coefficients calculated from Ali et al. (2016). It is worth noting that these recent radial diffusion models (Ali et al., 2016; Liu et al., 2016; Ozeke et al., 2014) are based on a separation of magnetic and electric field fluctuations made by Fei et al. (2006). As pointed out by Lejosne (2019), Fei et al.'s (2006) model for radial diffusion is erroneous because they separate delta E and delta B effects assuming that they have random phases which they do not for inductive ULF wave E and B fields. Lejosne (2019) finds that Fei et al.'s (2006) model, therefore all based on it, underestimate Fälthammar's (1965) D_{LL}^{B} by a factor of 2. Figure 1 shows the comparison of these aforementioned radial diffusion coefficients as a function of L^* at Kp = 1 and 5. The black, red, green, and blue lines show radial diffusion coefficients calculated using the above equations from Brautigam and Albert (2000), Ozeke et al. (2014), Ali et al. (2016), and Liu et al. (2016) (for a fixed value of μ = 700 MeV/G), respectively. It can be seen that, except for the outer boundary at L^* around 7, Ali et al. (2016) provide smaller radial diffusion coefficients than the other models. Similar comparisons of different radial diffusion coefficients have been made by other studies (e.g., Drozdov et al., 2017; Huang et al., 2010; Li et al., 2017, 2016). In these comparisons, radial diffusion coefficients from Brautigam and Albert (2000) are usually higher compared to other models during storm times. In particular, the radial diffusion coefficients from Brautigam and Albert (2000) and Ozeke et al. (2014) were tested in Drozdov et al. (2017) by performing long-term (1 year) simulation, and the results were similar. Note that in Drozdov et al. (2017) the outer boundary of the simulations was set up by using Van Allen Probe data at L^* = 5.5. In this study we set up the outer L^* boundary condition at L^* = 6.6. From Figure 1 it can be seen that, at higher Kp levels, the differences between the radial diffusion coefficient models are more significant at higher L^*, except for the model from Ali et al. (2016). Thus, comparing with the differences shown in Drozdov et al. (2017), larger differences between the results using radial diffusion coefficients from Brautigam and Albert (2000) and Ozeke et al. (2014) are expected from the higher outer L^* boundary.

2.2. Local Diffusion Coefficients

Bounce- and MLT-averaged diffusion coefficients D_{pp}, $D_{p\alpha_0}$, $D_{\alpha_0 p}$, and $D_{\alpha_0\alpha_0}$ are calculated using the Full Diffusion Code (Ni et al., 2008; Orlova & Shprits, 2011; Shprits & Ni, 2009; Shprits et al., 2009). The resonant diffusion coefficients are calculated for the resonant frequencies and wave numbers which satisfy the

dispersion relation of waves and the resonance condition

$$\omega - k_{\|} v_{\|} = n\Omega_e/\gamma, \tag{9}$$

where ω *is the wave frequency,* k is the wave number, v is the speed of particles, γ is the Lorentz factor, Ω_e is the gyro-frequency of electrons, and n is the order of the resonance. The Full Diffusion Code is capable of calculating resonant scattering rates including first-order ($n = 1$), Landau ($n = 0$), and higher order (higher n) resonance by obliquely propagating waves. For the bounce-average process, Orlova and Shprits (2011) developed a method for removing the integrand's singularity through a change of variables. The calculation of the diffusion coefficients requires wave models depending on spatial variables, such as MLT, latitude, L, and geomagnetic conditions. For the amplitude and frequency distribution of chorus waves, we use a newly developed model based on 5 years of Van Allen Probe data (Wang et al., 2019). For the wave normal angle (θ) distribution of chorus waves, we use a frequently adopted model, that is, $\theta_{lc} = 0°, \theta_{uc} = 45°, \theta_m = 0°$, and $\theta_w = 30°$, where θ_m is the peak value of wave normal angle, θ_w is the width of the angle, and θ_{lc} and θ_{uc} are the lower and upper cut-off to the wave normal angle distribution, outside which the wave power is zero (e.g., Kim et al., 2012; Thorne et al., 2013). For plasmaspheric hiss waves, we are also using a model developed based on Van Allen Probe observations (Orlova et al., 2016; Spasojevic et al., 2015). In this study, we assume local diffusion due to chorus waves outside the plasmasphere and due to hiss waves inside the plasmasphere. Plasma densities inside the plasmasphere are calculated according to Denton et al. (2006) and plasma densities outside the plasmasphere are estimated from Sheeley et al. (2001). We also include lightning whistlers with the same parameterization as in Kim et al. (2012). EMIC waves mainly affect electrons with energies higher than a few MeV. Therefore, effects of EMIC waves are not included in our simulations since we focus on the dynamics of electrons with energies of 0.9 MeV in this study. For the readers' interest, observations and simulations for 0.5 and 4 MeV electrons during these events are shown in the supporting material. It can be noted that without including EMIC waves, the simulations overestimate the flux of 4-MeV electrons. This indicates that including the effect of EMIC waves is needed for the simulations of 4-MeV electrons. The effect of EMIC waves during the GEM challenge events will be discussed in section 4.

2.3. Boundary and Initial Conditions

In our simulations, six boundary conditions and one initial condition are set up as follows:

- Lower L^* boundary: the PSD of electrons at the lower L^* boundary for the radial diffusion operator is set to be zero at $L^* = 1.0$ to represent losses to the atmosphere.
- Upper L^* boundary: the PSD variation at the outer boundary ($L^* = 6.6$) is calculated using GOES measurements, following the approach described in Wang and Shprits (2019).
- Boundary conditions for the pitch angle operator are $f(\alpha = 0.7°) = 0$ and $\partial f/\partial\alpha(\alpha = 89.3°) = 0$.
- For the energy diffusion operator, the electron PSD at the lower boundary is set to be constant at 10 keV at $L^* = 6.6$ and to extend to lower L^* to simulate a balance between convective sources and losses.
- The PSD at the upper energy boundary is set to be zero at 10 MeV at $L^* = 6.6$ assuming an absence of such high-energy electrons at $L^* = 6.6$.
- To focus on the GEM challenge events, we start the simulations 2 days before the events and set up the initial condition using 6 hr of the satellite data near the beginning of the simulation time.

2.4. Modeling Methodology

Technical details of the VERB-3D code can be found in previous studies (e.g., Castillo et al., 2019; Drozdov et al., 2017; Kim et al., 2012; Shprits et al., 2009; Subbotin et al., 2011). The numerical grid used in our simulations in this study is $29 \times 101 \times 91$, uniform in L^*, and logarithmic in energy and pitch angle. Several factors are taken into account in our simulations:

(1) The plasmapause location separates chorus waves outside of the plasmasphere and hiss waves inside the plasmasphere. We use two different methods to obtain the plasmapause position for each time step of the simulations. One method is to calculate the plasmapause position using the time series of the Kp index according to Carpenter and Anderson (1992):

$$L_{pp} = 5.6 - 0.46\mathrm{Kp}_{\max}, \tag{10}$$

where L_{pp} is the L-shell value of the plasmapause and Kp_{max} is the maximum Kp value over the previous 24 hr. This empirical plasmapause model is limited to a minimum $L_{\mathrm{pp}} = 2$ at $Kp_{max} \geq 7$. During the event

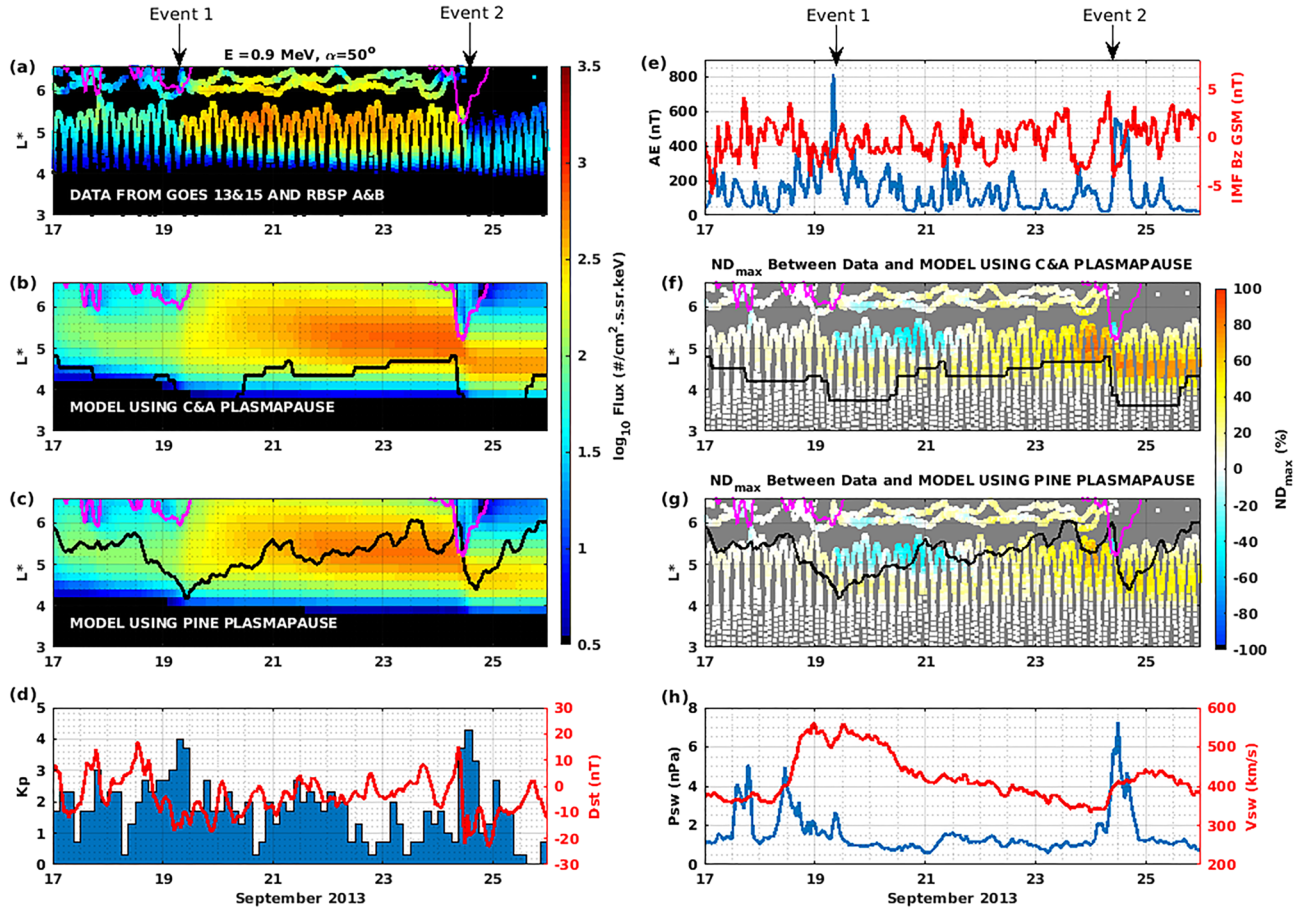

Figure 2. Electron flux observations, solar wind and geomagnetic conditions, and VERB simulations from 17 to 26 September 2013 including both nonstorm Geospace Environment Modeling challenge events (a nonstorm time enhancement event [Event 1] on 19 September 2013 and a nonstorm time dropout event [Event 2] on 24 September 2013). (a) Flux for 0.9 MeV, 50° pitch angle electrons from observations of Van Allen Probes, Geostationary Operational Environmental Satellites (GOES) 13 and 15. (b) VERB-3D simulation results using plasmapause positions calculated following Carpenter and Anderson (1992) for this period. (c) VERB-3D simulation results using the plasmapause position estimated from the new Plasma density in the Inner magnetosphere Neural network-based Empirical plasmasphere (PINE) model (Zhelavskaya et al., 2017). (d) Dst and Kp index during this period. (e) Auroral electrojet index and z-component of the interplanetary magnetic field (IMF Bz) in geocentric solar magnetic coordinates. (f) Normalized difference between observations (shown in Panel a) and simulations (shown in Panel b). (g) Normalized difference between observations (shown in Panel a) and simulations (shown in Panel c). (h) Solar wind dynamic pressure (nPa) and speed (km/s). The overplotted magenta lines in Panels (a)–(c) and (f)–(g) show the last closed drift shell. The overplotted black lines in Panels (b), (c), (f), and (g) show the plasmapause positions.

time periods under study here, the maximum Kp_{max} value is 7. The other method to obtain the plasmapause position is using the recently developed Plasma density in the Inner magnetosphere Neural network-based Empirical (PINE) model (Zhelavskaya et al., 2016, 2017, 2018). The PINE density model was developed using neural networks and was trained on the electron density data set from the Van Allen Probes Electric and Magnetic Field Instrument Suite and Integrated Science (Kletzing et al., 2013). The model reconstructs the plasmasphere dynamics well (with a cross-correlation of ~0.95 on the test set), and its global reconstructions of plasma density are in good agreement with the IMAGE extreme ultraviolet images of the global distribution of He^+. We compare the electron number density value given by the PINE model with the density threshold separating plasmaspheric-like and trough-like density given by Sheeley et al. (2001) and get the plasmapause position in each MLT. Then, we calculate the MLT-averaged plasmapause position. This data is available in Wang et al. (2020).

(2) The last closed drift shell (L^*_{LCDS}) is calculated using the International Radiation Belt Environment Modeling library (Boscher et al., 2010) and TS07D magnetic field model (Tsyganenko & Sitnov, 2007) and is then used to simulate the effect of magnetopause shadowing. When L^* is larger than the last closed drift shell location, we set the PSD to zero before the step of radial diffusion in the simulation.

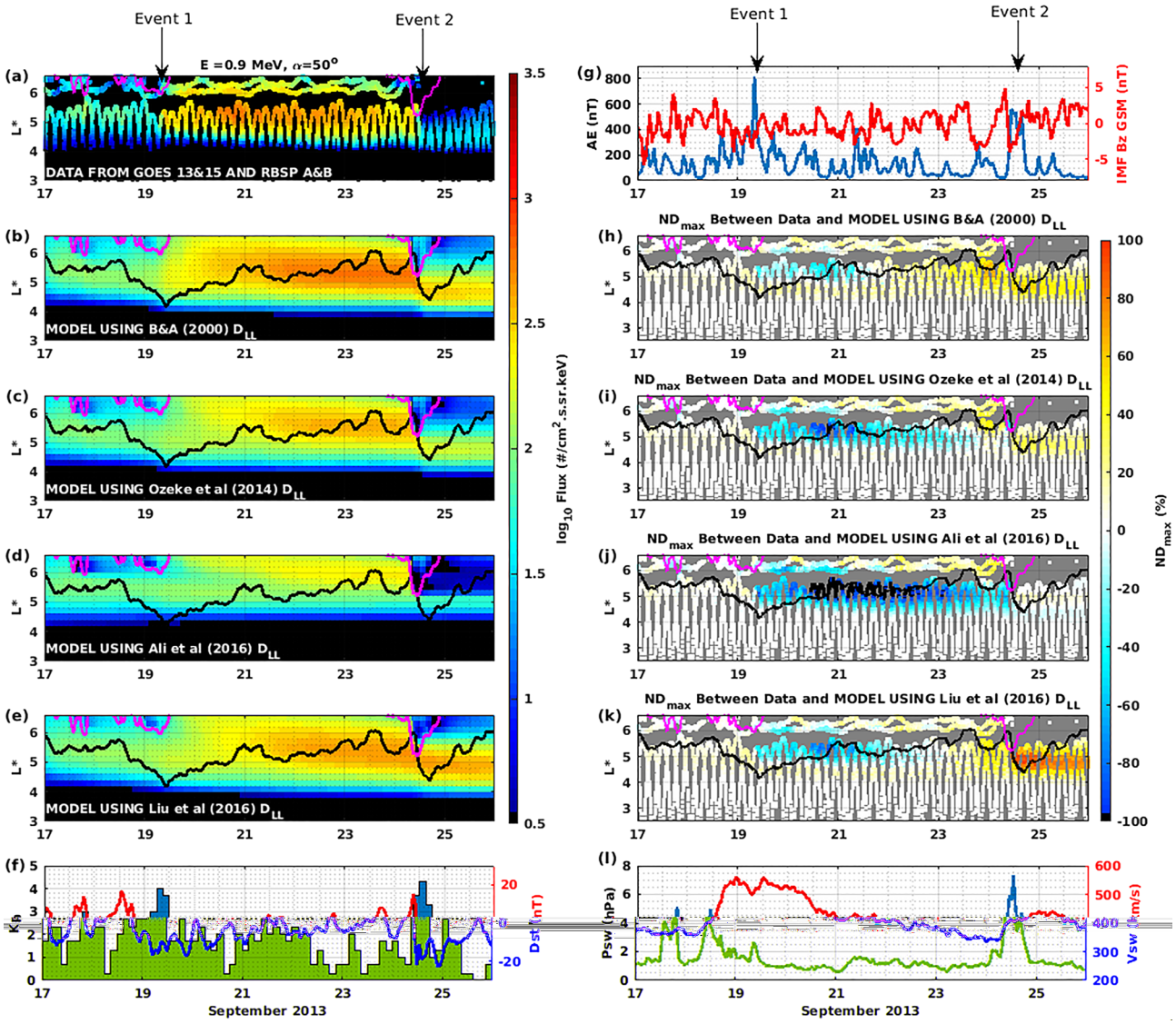

Figure 3. For the same events as shown in Figure 2, but testing different radial diffusion coefficient models. Panel (a) shows the flux from satellite observations for electrons at an energy of 0.9 MeV and equatorial pitch angle of 50° . Panels (b)–(e) show simulation results using different radial diffusion coefficients. Panels (f), (g), and (l) show the geomagnetic and solar wind conditions during this period. In Panels (h)–(k) we present the normalized differences between satellite data and results of simulations using different radial diffusion coefficients. Panels (a), (b), (f), (g), (h), and (l) in this figure are the same as Panels (a), (c), (d), (e), (g), and (h) in Figure 1. They are repeated in the figure for an easier comparison.

2.5. Validation Methodology

We validate our simulation results against satellite observations, which allows us to examine the extent to which the observed flux can be explained by the proposed mechanism and to test the effect of plasma boundaries. Particle measurements from both Van Allen Probes and GOES are used. The Magnetic Electron Ion Spectrometer instruments on board the Van Allen Probes measure electrons with energies from 20 keV to 4.8 MeV (Blake et al., 2013). To quantify the difference between the simulation results and the observations, we use the difference normalized by the maximum average of the observed flux (J_O) and simulated flux (J_S) for each 8 hr ($ND_{max}(L^*, t)$), which is defined as

$$\mathrm{ND}_{max}(L^*, t) = \frac{J_S(L^*, t) - J_O(L^*, t)}{\max|_{\text{over } L^* \text{ every 8 hours}} \frac{J_S(L^*, t) + J_O(L^*, t)}{2}}. \tag{11}$$

We choose 8 hr as a period for calculating the maximum average due to the fact that the Van Allen Probes fly through all L shells in approximately 8 hr.

3. Comparison of Simulations With Observations

In Figures 2–7, we compare the simulated fluxes to the observed fluxes from both Van Allen Probes and GOES, for the considered GEM challenge events. Figures 2, 4, and 6 show simulation results using different plasmapause positions for different events. In each of these figures, Panel (a) shows the observed flux of electrons with an energy of 0.9 MeV and an equatorial pitch angle of 50°, as a function of L^* and time. Here, L^* is calculated using the TS07D magnetic field model (Tsyganenko & Sitnov, 2007). Data from GOES and Van Allen Probes are consistent with each other at conjunction points. Panels (b) and (c) show the VERB-3D simulation results using plasmapause positions estimated following Carpenter and Anderson (1992) and calculated from the PINE plasmasphere model (Zhelavskaya et al., 2017), respectively. Panel (d) shows the geomagnetic Kp (blue steps) and Dst (red line) index. Panel (e) illustrates the geomagnetic auroral electrojet (AE) (red line) index and the z-component of the interplanetary magnetic field (IMF Bz) in the geocentric solar magnetic coordinate system. Panels (f) and (g) show the normalized differences between observations and simulation results using different plasmapause positions. The blue color indicates that the simulation results underestimate the flux, while red and yellow colors indicate that the simulation results overestimate the fluxes. The locations of the plasmapause are overplotted as black lines in Panels (b), (c), (f), and (g). The positions of the last closed drift shell calculated using the TS07D magnetic field model are overplotted as magenta lines in Panels (a)–(c) and (f)–(g). Panel (h) shows the solar wind speed (Vsw) (red line) and dynamic pressure (Psw) (blue line). We also performed simulations using different radial diffusion coefficients but the same plasmapause position calculated from the PINE model. Panels (b), (c), (d), and (e) in Figures 3, 5, and 7 show the simulation results using different radial diffusion coefficients, and Panels (h), (i), (j), and (k) in those figures show the normalized difference between those simulation results and satellite data. Panels (a), (f), (g), and (l) in Figures 3, 5, 7 are the same as Panels (a), (d), (e), and (h) in Figures 2, 4, and 6, respectively. These panels are repeated for easier comparison.

3.1. Events 1 and 2: Nonstorm Time Enhancement and Dropout

Figure 2 shows the electron flux observations, solar wind and geomagnetic conditions, and VERB-3D simulation results for the period from 17 to 26 September 2013, which includes two nonstorm GEM challenge events: a nonstorm time enhancement event (Event 1) on 20 September 2013 and a nonstorm time dropout event (Event 2) on 24 September 2013. These events are marked by arrows above Figure 2a. As shown in Figure 2h, before Event 1, during less than 1 day, the solar wind speed increased from lower than 400 km/s to higher than 550 km/s, and the solar wind dynamic pressure enhanced from lower than 2 nPa to higher than 4 nPa and then decreased to less than 2 nPa. Before Event 2, the solar wind dynamic pressure rose sharply to over 7 nPa and the solar wind speed increased gradually from 350 to 450 km/s. As shown in Figure 2e, close to Event 1, the IMF Bz changed direction from north to south and then fluctuated between north and south several times. Right before Event 1, the AE index sharply jumped from lower than 200 nT to higher than 800 nT, which indicates that a strong substorm was going on. Figure 2a illustrates that both GOES and Van Allen Probes observed a significant enhancement of relativistic electrons on 19–20 September 2013, which is followed by a dropout at higher L shells ($L^* > 5$) and a moderate decrease near L^* of 5 on 24 September 2013 (Event 2). Figure 2b shows simulation results using the plasmapause positions estimated following Carpenter and Anderson (1992). It can be seen from Figure 2f that the simulation reproduces the enhancement of relativistic electron flux in the heart of the belt but underestimates the flux at an L^* range from 5 to 5.5 during Event 1. After 21 September, the simulation overestimates the flux. The overestimation can be associated with the plasmapause location. Outside the plasmapause, chorus wave acceleration leads to overestimation. It can be seen from Figures 2c and 2g that using the new plasmapause location improves the agreement between observations and simulations significantly. There is still some overestimation, which may result from the diffusion coefficients of hiss waves. For the dropout event (Event 2) on 24 September, the dropout at higher L shells is reproduced in both simulations by involving the magnetopause shadowing effect. However, a decrease of flux at an L-shell range from 4 to 5 is not well reproduced, which will be discussed in section 4.

Figure 3 shows the results of simulations using different radial diffusion coefficients but the same plasmapause positions, which are calculated from the PINE plasmasphere model. It can be seen that the results of the simulations using the radial diffusion coefficients from Brautigam and Albert (2000) produces the best agreement with observations during Event 1. Other models produce more underestimations. In particular, simulation results using the radial diffusion coefficients from Ali et al. (2016) produce the most significant underestimations, which can be seen in Figure 3j. As shown in Figure 1, the radial diffusion coefficients

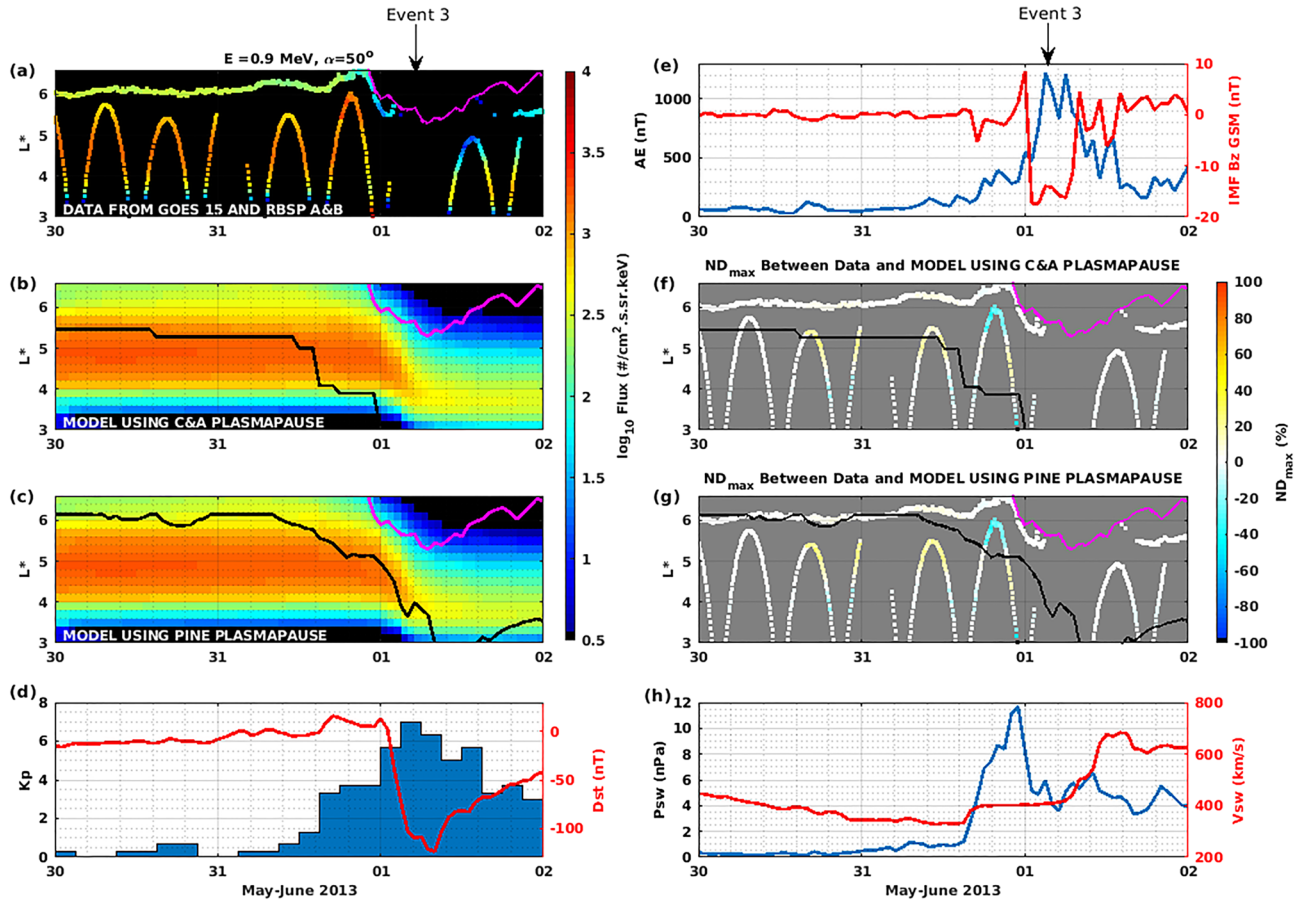

Figure 4. Same format as Figure 2 but for Event 3 (the storm time dropout Geospace Environment Modeling challenge event on 1 June 2013) from 30 May to 2 June 2013.

from Ali et al. (2016) are lower than other radial diffusion coefficients except at the outer boundary. The simulation outcome for Event 2 is affected by the simulation results before this event. For example, simulation results using D_{LL} from Ali et al. (2016) produce an underestimation during Event 2 due to the underestimation before Event 2. Simulation results using D_{LL} from Liu et al. (2016) show deeper underestimation during Event 1 and higher overestimation during Event 2. Simulations using D_{LL} from Ozeke et al. (2014) also produce deeper underestimation compared to the simulations using D_{LL} from Brautigam and Albert (2000) during Event 1.

3.2. Event 3: Storm Time Dropout

Right before 1 June 2013, the solar wind dynamic pressure increased sharply from less than 2 nPa to near 12 nPa in less than half a day, as shown in Figure 4h. The solar wind speed gradually increased from 400 km/s to around 700 km/s during Event 3 (Figure 4h). On 1 June 2013, the IMF Bz had a strong southward excursion with an amplitude higher than 15 nT, and the AE index was sharply enhanced from lower than 500 nT to around 1,400 nT, indicating that a strong substorm happened (Figure 4e). As shown in Figure 4d, a strong geomagnetic storm happened with a minimum Dst index of −110 nT and a maximum Kp index of 7 on 1 June 2013. An electron flux dropout occurred on 1 June 2013, as shown in Figure 4a. During this period, GOES 13 data is not available. However, GOES 15 data is available, as shown in Figure 4a. Panels (b) and (c) show results of VERB-3D simulations using different plasmapause positions (overplotted as black lines). The overplotted magenta lines give the LCDS locations calculated in the TS07D magnetic field model. It can be seen, using the positions of the LCDS, that the simulation can reproduce the dropouts outside the LCDS well. The simulation results using different plasmapause positions are similar. The reasons for this similarity will be discussed in section 4.

Figure 5 shows the simulation results using different radial diffusion coefficient (D_{LL}) models for Event 3. Before the storm, geomagnetic conditions were very quiet. As shown in Figure 1, the differences between

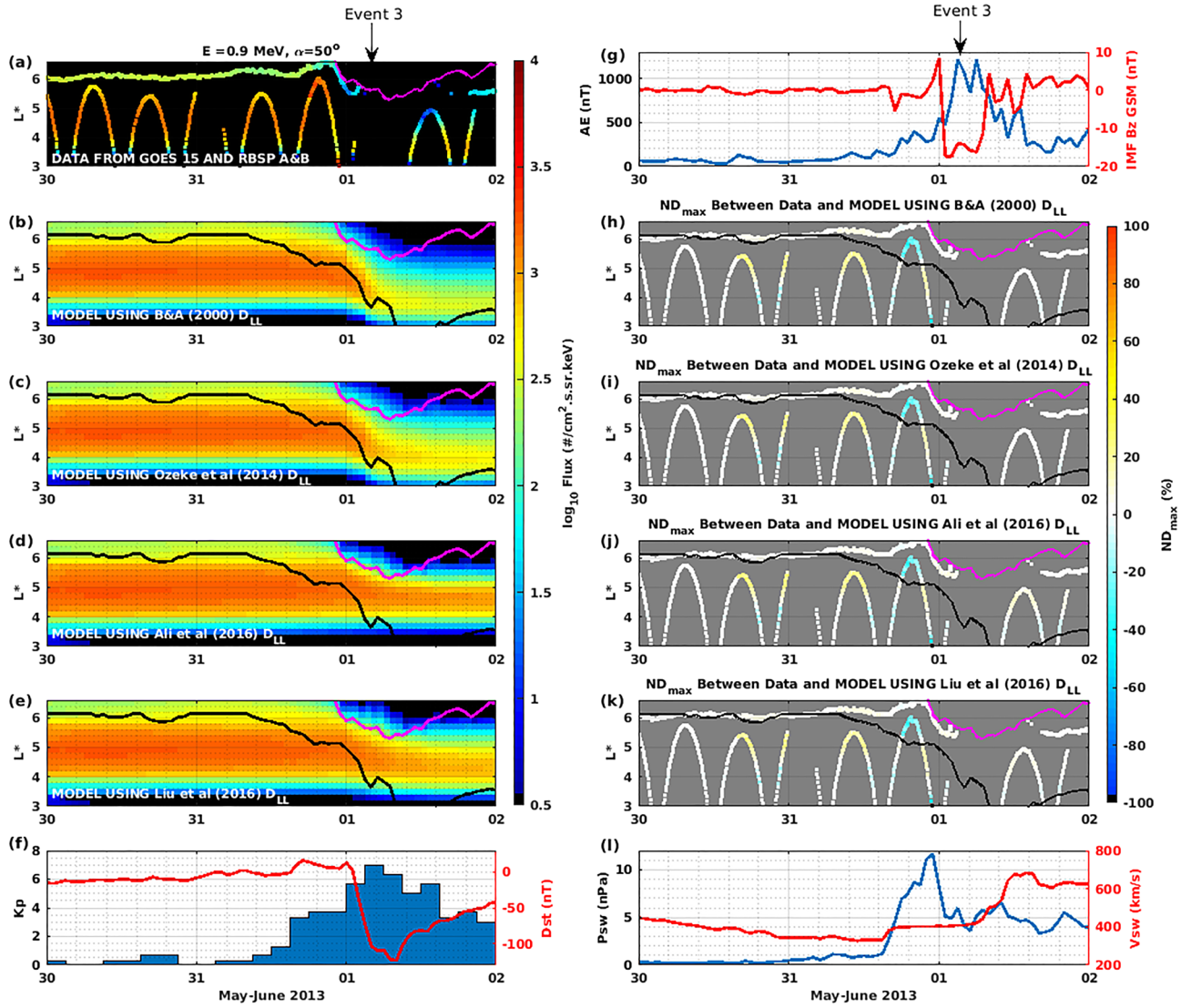

Figure 5. Comparison of simulation results using different radial diffusion coefficient models for Event 3. Same format as in Figure 3.

different D_{LL} are not so significant. During the storm, as the LCDS were pushed into the geosynchronous orbit, the dominant loss mechanism was loss to the magnetopause and outward radial diffusion. Radial diffusion coefficients from Ali et al. (2016) are the smallest during the storm and simulation results using these diffusion coefficients leave the strongest remnant belt at L^* from 4 to 5.

3.3. Event 4: Storm Time Enhancement

On 17 March 2013, a strong storm occurred with a minimum *Dst* index of −132 nT and a maximum Kp index of 7-, as shown in Figure 6d. Before the storm, several substorms happened during 16 March 2013, as indicated by the AE index in Figure 6e. Seed electrons can be injected during these substorms. On 17 March, a stronger substorm happened with an AE index higher than 1,700 nT. IMF Bz became southward several times and with the southward amplitude increasing to more than 10 nT. The solar wind dynamic pressure jumped from 1 nPa to higher than 12 nPa and solar wind speed increased from around 400 to 700 km/s within 5 hr. These solar wind and geomagnetic activities caused the LCDS to move into the geosynchronous orbit and to approach L^* as low as 5 (indicated by magenta lines in Figures 6a–6c). Before 12:00 UT on 17 March, the fluxes of relativistic electrons were dramatically depleted, especially at high L shells ($L^* \geq 5$). This depletion is suggested to result from the magnetopause shadowing effect (Baker et al., 2014; Li et al., 2014; Olifer et al., 2018). However, previous simulation studies for this event did not investigate the effect of

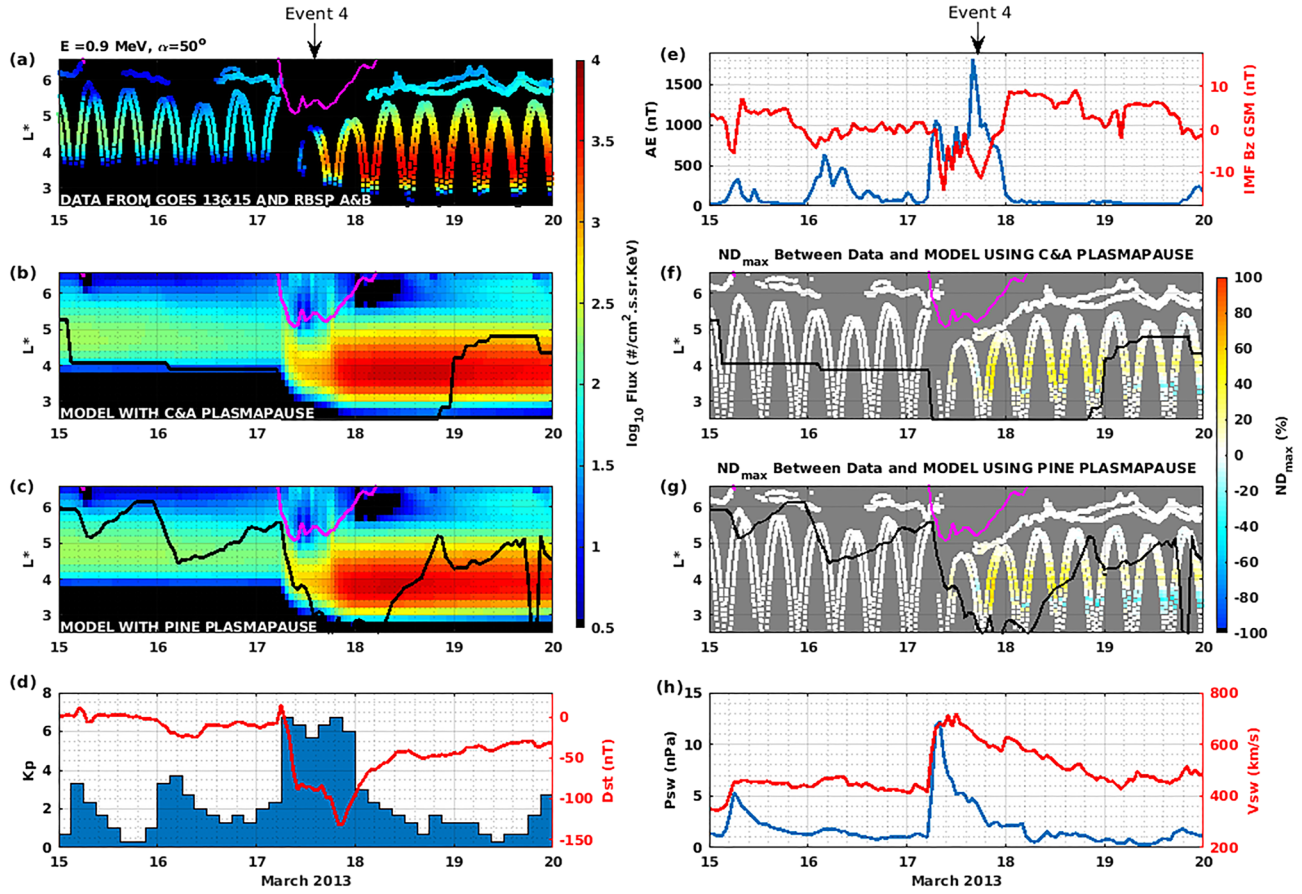

Figure 6. Same format as Figure 2 but for Event 4 (the storm time enhancement Geospace Environment Modeling challenge event on 17 March 2013) from 15 to 20 March 2013.

magnetopause shadowing. After this sharp dropout across a wide L^* range, the flux of relativistic electrons recovered and enhanced significantly by 2 orders of magnitude at L^* from 3 to 5, as shown in Figure 6a.

In our simulations, we include the effect of magnetopause shadowing to investigate the reason for the sharp dropout before the enhancement event and test the influence of the different plasmapause positions. In addition, instead of using event-specific chorus waves from observations, in our simulations, we use a statistical chorus wave model which was developed using 5 years of Van Allen Probe data (Wang et al., 2019). Figures 6b and 6c show the results of VERB-3D simulations using different plasmapause positions. As can be seen in these figures, the depletion of electron fluxes can be reproduced well by the loss to the LCDS (indicated by the overplotted magenta lines). After this depletion, the flux of relativistic electrons is enhanced by nearly two orders of magnitude during the 12 hr interval on 17 March in the L-shell range [3, 5]. The peak location of the outer radiation belt moves toward the Earth compared to the location before this storm. The simulation results indicate that the enhancement of relativistic electrons is well reproduced. Simulation results using a different plasmapause location during Event 4 show no significant differences, which will be discussed in section 4.

Figure 7 shows the simulation results using different radial diffusion coefficient models. It can be readily seen from this figure that the simulation using radial diffusion coefficients from Brautigam and Albert (2000) produces the best agreement between simulation results and satellite observations. Simulations using other radial diffusion coefficients underestimate the flux enhancement of relativistic electrons during Event 4. At such high Kp levels in Event 4 (maximum Kp = 7), the diffusion coefficients from Brautigam and Albert (2000) are much higher than others, especially at high L^*.

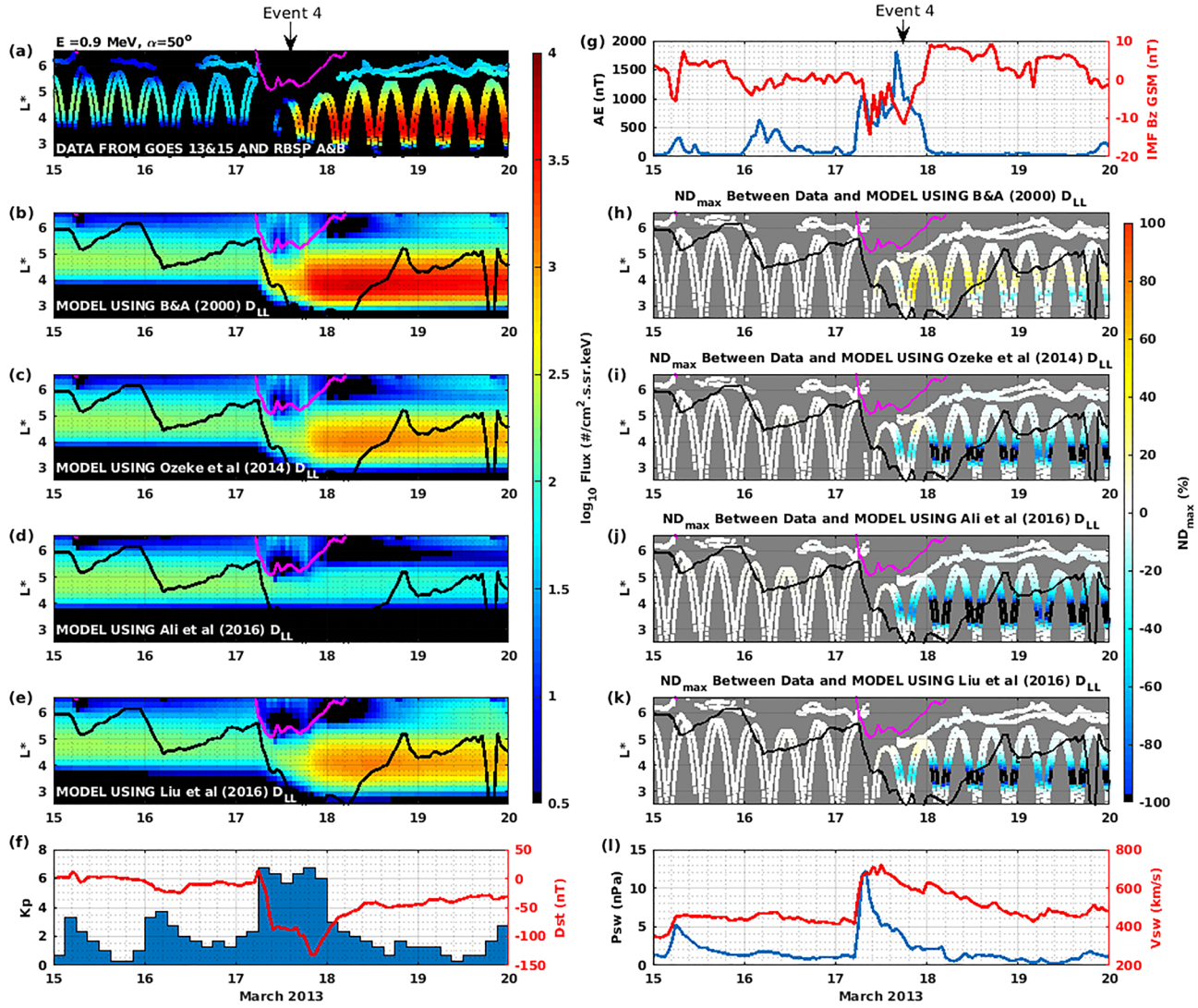

Figure 7. Test of the sensitivity of different radial diffusion coefficients. Same format as Figure 3 but for the Geospace Environment Modeling challenge Event 4 (the storm time enhancement Geospace Environment Modeling challenge event on 17 March 2013) from 15 to 20 March 2013.

4. Discussion

4.1. Solar wind and Geomagnetic Indices for the Dynamic Evolution of Radiation Belt Electrons

The enhancement and the dropout events (Events 1 and 2) during the end of September 2013 have been selected by the GEM Focus Group Quantitative Assessment of Radiation Belt Modeling as nonstorm time challenge events based on the Dst index. However, the Kp index increased to 4 at both enhancement and dropout time. As discussed in Borovsky and Shprits (2017), much of the dynamics of the radiation belts is better organized by the Kp index, rather than by the Dst index. Both Events 1 and 2 experienced decrease in Dst and increase in Kp, but the changes during Event 2 were more abrupt. Comparing the solar wind condition during these events, Event 1 experienced a higher solar wind speed but a less significant increase of solar wind dynamic pressure. During both Events 1 and 2, the IMF Bz had a southward excursion but the IMF Bz stayed southward for a longer time period in Event 2 than it did in Event 1. These solar wind conditions resulted in the lower LCDS in Event 2 in contrast to Event 1. The AE index in Event 1 had a sharper and more significant enhancement than that in Event 2, which implies that the substorm-related injection of electrons is stronger in Event 1 than that in Event 2. All these factors result in the enhancement in Event 1, but the dropout in Event 2.

Comparing Events 3 and 4, the geomagnetic storm in Event 4 is stronger than the storm in Event 3. The Dst index decreased to a lower value (−132 nT) in Event 4 than in Event 3 (−124 nT). The Kp index increased

more abruptly and stayed longer at Kp = 7 in Event 4 than it did in Event 3. Before Event 3, the geomagnetic activity was relatively quiet compared to the geomagnetic activity before Event 4. The solar wind speed enhancement happened before Event 4 but during Event 3. In addition, the solar wind speed jumped more abruptly before Event 4 than it did during Event 3. Before the enhancement in Event 4, the solar wind speed increased from 400 to 700 km/s in less than 5 hr. During Event 3, the solar wind speed increased from 400 to 700 km/s during 10 hr. During Event 4, the solar wind speed increased simultaneously with dynamic pressure. However, during Event 3, the significant enhancement of solar wind speed occurred more than half a day later after the enhancement of solar wind dynamic pressure. These different solar wind and geomagnetic conditions result in different responses of radiation belt electrons.

4.2. Effect of EMIC Waves During the GEM Challenge Events

The current study focuses on the dynamic evolution of electrons at an energy of 0.9 MeV, which are in general not significantly affected by EMIC waves. However, considering the interest in the effect of EMIC waves on the radiation belt electrons, especially for these GEM challenge events, here we discuss the effect of EMIC waves during these events. We also show the results of the simulations without EMIC waves for 500-keV and 4-MeV electrons in the supporting material and compare them with satellite observations. In general, without taking EMIC waves into account, our simulations reproduce the dynamic evolution of electrons at energies of 500 and 900 keV well but overestimated the flux of electrons with energies of 4 MeV in Events 1, 2, 3, during which intense EMIC waves were observed (Engebretson et al., 2018). These results indicate a missing loss mechanism for ultrarelativistic electrons, which is consistent with previous studies (e.g., Drozdov et al., 2015).

In particular, several studies have investigated the effect of EMIC waves in Event 2. During several hours on 24 September 2013 during Event 2, the radiation belt electrons with energies from 500 keV to several MeV exhibited a significant dropout at higher L shells ($L^* > 5$) and a moderate decrease near L^* of 5. For 0.9-MeV electrons, our simulations incorporate the magnetopause shadowing effect by using the LCDS and reproduce the dropout at higher L shells. However, the decrease of flux of electrons at an energy of 0.9 MeV at an L-shell range from 4 to 5 is not well reproduced. This may result from an underestimation of outward radial diffusion or a lack of wave-particle interactions in plasmaspheric plumes. On the other hand, EMIC waves are observed during the interval of this dropout event (Event 2). Comparing Figure 2 for the 900-keV electrons with Figure S1 for 500-keV electrons and S2 for 4-MeV electrons, it can be seen that more significant overestimations are produced for the flux of higher-energy electrons. The simulation with PINE plasmapause reproduces the dynamic evolution of 500-keV electrons well (Figure S1) but overestimate the flux of electrons at energies of 0.9 and 4 MeV. Su et al. (2016) suggested that this dropout is mainly caused by wave-induced precipitation by plasmaspheric hiss waves and EMIC waves. Using a cold plasma approximation and setting the upper cut-off frequency of EMIC waves at $0.98 f_{\mathrm{cHe^+}}$, the minimum resonant energy of electrons were calculated to extend to as low as 400 keV in their study. Using conjugate observations from Van Allen Probe A and MetOp-01 satellites, Capannolo et al. (2018) reported coincident observations of EMIC waves and precipitation of electrons with energies extending to even tens of keV during Event 2. By setting up the upper cut-off frequency at $0.99 f_{cH}$ and $0.99 f_{cHe}$ for H-band and He-band EMIC waves, respectively, Capannolo et al. (2018) calculated the quasi-linear pitch angle diffusion coefficients due to EMIC waves based on cold plasma approximation. Their results show that the minimum resonant energy of electrons that can be scattered by H-band EMIC waves can extend to tens of keV, although the diffusion coefficients are much lower than those for high-energy electrons. By using multi-instrument observations and nonlinear test particle simulations following (Omura & Zhao, 2012, 2013), Hendry et al. (2019) suggested that EMIC waves can cause the sub-MeV electron precipitation. However, taking hot plasma effects into account, the minimum resonance energies of electrons interacting with EMIC waves are found to be generally higher than 1 MeV (Cao et al., 2017). By analyzing the wave number of observed EMIC waves and calculating the minimum resonance energy, Chen et al. (2019) found that during this event, the minimum resonance energy between EMIC waves and electrons is higher than 16 MeV (see their supporting information). Thus, the effects of EMIC waves in this dropout event are still under debate. Using satellite and ground observations, Engebretson et al. (2018) investigated EMIC waves and their effect on radiation belt electrons for these GEM challenge events. They also investigated PSD and pitch angle distributions of electrons for Event 2 in this study. The dips in PSD are suggested to be a signature of EMIC-caused precipitations (e.g., Aseev et al., 2017; Shprits et al., 2017). Dips in the PSD profile were found for electrons with energies higher than 2 MeV ($\mu = 3,500$ MeV/G and $K = 0.1$ $\mathrm{G}^{0.5}\mathrm{R_E}$ between $L^* = 3.4$ and 5.4, see their Figure 8), but

no dips in PSD were found for electrons with energies near 1 MeV (μ = 700 MeV/G and K = 0.1 $G^{0.5}R_E$, see their Figure S2) in Event 2. The investigation of the electron depletion at low L shell during this event will be the subject of future research.

4.3. Parameterization of Radial Diffusion Coefficients

An underestimation of the radial diffusion coefficients can result in an underestimation of the loss caused by magnetopause shadowing accompanied with outward radial diffusion at higher L^* or an underestimation of inward radial diffusion and flux at lower L^*. Olifer et al. (2019) showed that empirical Kp-dependent radial diffusion coefficient models can underestimate radial diffusion, especially during intervals with southward IMF. During the events studied here, the overestimation of the flux during Event 2 possibly results from the underestimation of outward radial diffusion, considering the IMF Bz changed to southward for several hours (Figure 2e). In addition, the underestimation of flux at $L^* = 3.5$ during Event 4 in the recovery phase of the storm probably results from the underestimation of inward radial diffusion. However, Drozdov et al. (2017) showed that the multiplication of the radial diffusion coefficients by a constant factor can push the inner boundary of the outer radiation belt to unrealistic positions. Performing simulations using event-specific radial diffusion coefficients is beyond the scope of the current study. Another possibility for this underestimation is that local heating shown to be important for Event 4 (e.g., Castillo et al., 2019; Li et al., 2014; Shprits et al., 2015; Xiao et al., 2014) may be stronger than modeled.

4.4. Parameterization of Plasmapause Position

For the nonstorm GEM challenge events (Events 1 and 2), using the parameterization of plasmapause from the PINE model produces clearly better agreement with satellite observations, as shown in Figure 2. However, this improvement is not very significant during storm times (Events 3 and 4, as shown in Figures 4 and 6). During storm times, the plasmasphere becomes more asymmetric due to the enhanced convection (e.g., Goldstein et al., 2005). During storm times, the plasmasphere is strongly eroded at all MLTs except for the dusk sector, where a bulge or plume is formed and extends further to the noon sector. A plasmaspheric bulge or plumes may form and extend to higher L shells during storm time. However, in our 3D simulations using the PINE output, the plasmapause positions are averaged over MLT. This may lead to some overestimation of plasmapause positions during storm times, which can lead to an underestimation of the acceleration by chorus waves. In addition, our simulations in this study did not account for hiss waves in the plasmaspheric plume, which may cause some underestimation of losses.

5. Summary and Conclusions

In this study, we perform simulations for GEM challenge events using the VERB-3D code. Magnetopause shadowing effect are included in the simulations by using the last closed drift shells. We perform simulations using different plasmapause positions and four different radial diffusion coefficient models. The results of our study show that

1. The magnetopause shadowing effect plays an important role for dropout at higher L shells. The last closed drift shell calculated using the TS07D magnetic field model can be used to simulate the magnetopause shadowing effect.
2. The position of the plasmapause plays an important role in the dynamic evolution of radiation belt electrons, especially during nonstorm times.
3. Flux measurements from GOES observations can be used to set up outer boundary conditions for the simulation of radiation belts. During times when the Van Allen Probes data is not available, we can still use measurements from GOES to set up outer boundaries and infer the radiation belt dynamics at lower L shells.
4. Simulations using radial diffusion coefficients calculated from Brautigam and Albert (2000) produces the best agreement between satellite observations and simulation results for these events.

In future studies, we will test the usage of the innermost position of the plasmapause and include plumes by changing the MLT percentage of chorus waves and hiss waves in different time steps of the simulations. Additionally, 4D simulations including the MLT dependence will be performed to check the effect of the MLT-dependent plasmapause position and plasmaspheric plumes on the dynamic evolution of the radiation belts in detail.

Abbreviations

GEM	Geospace Environment Modeling
VERB-3D code	3-Dimensional Versatile Electron Radiation Belt code
MLT	Magnetic Local Time
PSD	Phase Space Density
IMF	Interplanetary Magnetic Field
LCDS	Last Closed Drift Shell
FDC	Full Diffusion Code
PINE	Plasma density in the Inner magnetosphere Neural network-based Empirical model

Acknowledgments
We acknowledge the Geospace Environment Modeling Focus Group on the "Quantitative Assessment of Radiation Belt Modeling" for motivating this study. We sincerely acknowledge Adam Kellerman for the preparation of the satellite data used and the calculation of the last closed drift shells. We would like to thank Hayley Allison for the useful discussions. This project has received funding from the European Union's Horizon 2020 research and innovation program under Grant 637302 (PROGRESS), 870452 (PAGER), NASA H-SR Funding NNX15AI94G, and the Helmholtz-Gemeinshaft (HGF) [https://doi.org/10.13039/501100001656]. I. Z. was supported by Geo.X, the Research Network for Geosciences in Berlin and Potsdam, under Grant SO-087-GeoX. A. D. also acknowledges support from NASA Grant 80NSSC18K0663. All Van Allen Probes data were accessed through the MagEIS website (https://rbsp-ect.lanl.gov), and we graciously thank the MagEIS instrument team. The Kp index was provided by GFZ section 2.3 and downloaded from the World Data Center (http://wdc.kugi.kyoto-u.ac.jp/). The MLT-averaged plasmapause position is available in Wang et al. (2020).

References

Ali, A. F., Malaspina, D. M., Elkington, S. R., Jaynes, A. N., Chan, A. A., Wygant, J., & Kletzing, C. A. (2016). Electric and magnetic radial diffusion coefficients using the Van Allen probes data. *Journal of Geophysical Research: Space Physics*, *121*, 9586–9607. https://doi.org/10.1002/2016JA023002

Aseev, N. A., Shprits, Y. Y., Drozdov, A. Y., Kellerman, A. C., Usanova, M. E., Wang, D., & Zhelavskaya, I. S. (2017). Signatures of ultra-relativistic electron loss in the heart of the outer radiation belt measured by Van Allen Probes. *Journal of Geophysical Research: Space Physics*, *122*, 10,102–10,111. https://doi.org/10.1002/2017JA024485

Aseev, N. A., Shprits, Y. Y., Wang, D., Wygant, J., Drozdov, A. Y., Kellerman, A. C., & Reeves, G. D. (2019). Transport and loss of ring current electrons inside geosynchronous orbit during the 17 March 2013 storm. *Journal of Geophysical Research: Space Physics*, *124*, 915–933. https://doi.org/10.1029/2018JA026031

Baker, D. N., Jaynes, A. N., Li, X., Henderson, M. G., Kanekal, S. G., Reeves, G. D., et al. (2014). Gradual diffusion and punctuated phase space density enhancements of highly relativistic electrons: Van Allen Probes observations. *Geophysical Research Letters*, *41*, 1351–1358. https://doi.org/10.1002/2013GL058942

Blake, J., Carranza, P., Claudepierre, S., Clemmons, J., Crain, W., Dotan, Y., et al. (2013). The Magnetic Electron Ion Spectrometer (MagEIS) instruments aboard the radiation belt storm probes (RBSP) spacecraft. *Space Science Reviews*, *179*, 383–421. https://doi.org/10.1007/s11214-013-9991-8

Borovsky, J. E., & Shprits, Y. Y. (2017). Is the Dst index sufficient to define all geospace storms? *Journal of Geophysical Research: Space Physics*, *122*, 11,543–11,547. https://doi.org/10.1002/2017JA024679

Boscher, D., Bourdarie, S., O'Brien, P., & Guild, T. (2010). IRBEM library v4. 3, 2004–2008. ONERA-DESP, Toulouse France, Aerospace Corporation, Washington, DC.

Boyd, A. J., Spence, H. E., Claudepierre, S. G., Fennell, J. F., Blake, J. B., Baker, D. N., et al. (2014). Quantifying the radiation belt seed population in the 17 March 2013 electron acceleration event. *Geophysical Research Letters*, *41*, 2275–2281. https://doi.org/10.1002/2014GL059626

Brautigam, D. H., & Albert, J. M. (2000). Radial diffusion analysis of outer radiation belt electrons during the October 9, 1990, magnetic storm. *Journal of Geophysical Research*, *105*(A1), 291–309. https://doi.org/10.1029/1999JA900344

Cao, X., Shprits, Y. Y., Ni, B., & Zhelavskaya, I. S. (2017). Scattering of ultra-relativistic electrons in the Van Allen radiation belts accounting for hot plasma effects. *Scientific Reports*, *7*(1), 17,719.

Capannolo, L., Li, W., Ma, Q., Zhang, X.-J., Redmon, R. J., Rodriguez, J. V., et al. (2018). Understanding the driver of energetic electron precipitation using coordinated multisatellite measurements. *Geophysical Research Letters*, *45*, 6755–6765. https://doi.org/10.1029/2018GL078604

Carpenter, D., & Anderson, R. (1992). An ISEE/whistler model of equatorial electron density in the magnetosphere. *Journal of Geophysical Research*, *97*(A2), 1097–1108.

Castillo, A. M., Shprits, Y. Y., Ganushkina, N., Drozdov, A., Aseev, N., Wang, D., & Dubyagin, S. (2019). Simulations of the inner magnetospheric energetic electrons using the IMPTAM-VERB coupled model. *Journal of Atmospheric and Solar-Terrestrial Physics*, *191*, 105050. https://doi.org/10.1016/j.jastp.2019.05.014

Chen, Y., Reeves, G. D., Friedel, R. H., & Cunningham, G. S. (2014). Global time-dependent chorus maps from low-Earth-orbit electron precipitation and Van Allen Probes data. *Geophysical Research Letters*, *41*, 755–761. https://doi.org/10.1002/2013GL059181

Chen, L., Zhu, H., & Zhang, X. (2019). Wavenumber analysis of EMIC waves. *Geophysical Research Letters*, *46*, 5689–5697. https://doi.org/10.1029/2019GL082686

Denton, R., Takahashi, K., Galkin, I., Nsumei, P., Huang, X., Reinisch, B., et al. (2006). Distribution of density along magnetospheric field lines. *Journal of Geophysical Research*, *111*, A04213. https://doi.org/10.1029/2005JA011414

Drozdov, A., Shprits, Y., Aseev, N., Kellerman, A., & Reeves, G. D. (2017). Dependence of radiation belt simulations to assumed radial diffusion rates tested for two empirical models of radial transport. *Space Weather*, *15*, 150–162. https://doi.org/10.1002/2016SW001426

Drozdov, A. Y., Shprits, Y. Y., Orlova, K. G., Kellerman, A. C., Subbotin, D. A., Baker, D. N., et al. (2015). Energetic, relativistic, and ultrarelativistic electrons: Comparison of long-term verb code simulations with van allen probes measurements. *Journal of Geophysical Research: Space Physics*, *120*, 3574–3587. https://doi.org/10.1002/2014JA020637

Drozdov, A., Shprits, Y., Usanova, M., Aseev, N., Kellerman, A., & Zhu, H. (2017). EMIC wave parameterization in the long-term VERB code simulation. *Journal of Geophysical Research: Space Physics*, *122*, 8488–8501. https://doi.org/10.1002/2017JA024389

Engebretson, M., Posch, J., Braun, D., Li, W., Ma, Q., Kellerman, A., et al. (2018). EMIC wave events during the four GEM QARBM challenge intervals. *Journal of Geophysical Research: Space Physics*, *123*, 6394–6423. https://doi.org/10.1029/2018JA025505

Fälthammar, C.-G. (1965). Effects of time-dependent electric fields on geomagnetically trapped radiation. *Journal of Geophysical Research*, *70*(11), 2503–2516. https://doi.org/10.1029/JZ070i011p02503

Fei, Y., Chan, A. A., Elkington, S. R., & Wiltberger, M. J. (2006). Radial diffusion and MHD particle simulations of relativistic electron transport by ULF waves in the September 1998 storm. *Journal of Geophysical Research*, *111*, A12209. https://doi.org/10.1029/2005JA011211

Foster, J., Erickson, P., Baker, D., Claudepierre, S., Kletzing, C., Kurth, W., et al. (2014). Prompt energization of relativistic and highly relativistic electrons during a substorm interval: Van Allen Probes observations. *Geophysical Research Letters*, *41*, 20–25. https://doi.org/10.1002/2013GL058438

Foster, J., Erickson, P., Omura, Y., Baker, D., Kletzing, C., & Claudepierre, S. (2017). Van Allen Probes observations of prompt MeV radiation belt electron acceleration in nonlinear interactions with VLF chorus. *Journal of Geophysical Research: Space Physics*, *122*, 324–339. https://doi.org/10.1002/2016JA023429

Fu, H., Cao, J., Yang, B., & Lu, H. (2011). Electron loss and acceleration during storm time: The contribution of wave-particle interaction, radial diffusion, and transport processes. *Journal of Geophysical Research*, *116*, A10210. https://doi.org/10.1029/2011JA016672

Goldstein, J., Sandel, B. R., Forrester, W. T., Thomsen, M. F., & Hairston, M. R. (2005). Global plasmasphere evolution 22-23 April 2001. *Journal of Geophysical Research*, *110*, A12218. https://doi.org/10.1029/2005JA011282

Gu, X., Shprits, Y. Y., & Ni, B. (2012). Parameterized lifetime of radiation belt electrons interacting with lower-band and upper-band oblique chorus waves. *Geophysical Research Letters*, *39*, L15102. https://doi.org/10.1029/2012GL052519

Hendry, A. T., Santolik, O., Kletzing, C. A., Rodger, C. J., Shiokawa, K., & Baishev, D. (2019). Multi-instrument observation of nonlinear EMIC-driven electron precipitation at sub-MeV energies. *Geophysical Research Letters*, *46*, 7248–7257. https://doi.org/10.1029/2019GL082401

Horne, R. B., & Thorne, R. M. (1998). Potential waves for relativistic electron scattering and stochastic acceleration during magnetic storms. *Geophysical Research Letters*, *25*(15), 3011–3014.

Horne, R., & Thorne, R. (2003). Relativistic electron acceleration and precipitation during resonant interactions with whistler-mode chorus. *Geophysical Research Letters*, *30*(10), 1527. https://doi.org/10.1029/2003GL016973

Huang, C.-L., Spence, H. E., Hudson, M. K., & Elkington, S. R. (2010). Modeling radiation belt radial diffusion in ULF wave fields: 2. Estimating rates of radial diffusion using combined MHD and particle codes. *Journal of Geophysical Research*, *115*, A06216. https://doi.org/10.1029/2009JA014918

Hudson, M., Paral, J., Kress, B., Wiltberger, M., Baker, D., Foster, J., et al. (2015). Modeling CME-shock-driven storms in 2012–2013: MHD test particle simulations. *Journal of Geophysical Research: Space Physics*, *120*, 1168–1181. https://doi.org/10.1002/2014JA020833

Kang, S.-B., Fok, M.-C., Komar, C., Glocer, A., Li, W., & Buzulukova, N. (2018). An energetic electron flux dropout due to magnetopause shadowing on 1 June 2013. *Journal of Geophysical Research: Space Physics*, *123*, 1178–1190. https://doi.org/10.1002/2017JA024879

Kim, H.-J., & Chan, A. A. (1997). Fully adiabatic changes in storm time relativistic electron fluxes. *Journal of Geophysical Research*, *102*, 22,107–22,116.

Kim, K.-C., Shprits, Y., Subbotin, D., & Ni, B. (2012). Relativistic radiation belt electron responses to GEM magnetic storms: Comparison of CRRES observations with 3-D VERB simulations. *Journal of Geophysical Research*, *117*, A08221. https://doi.org/10.1029/2011JA017460

Kletzing, C., Kurth, W., Acuna, M., MacDowall, R., Torbert, R., Averkamp, T., et al. (2013). The electric and magnetic field instrument suite and integrated science (EMFISIS) on RBSP. *Space Science Reviews*, *179*(1-4), 127–181.

Kubota, Y., & Omura, Y. (2018). Nonlinear dynamics of radiation belt electrons interacting with chorus emissions localized in longitude. *Journal of Geophysical Research: Space Physics*, *123*, 4835–4857. https://doi.org/10.1029/2017JA025050

Lanzerotti, L. J., & Morgan, C. G. (1973). ULF geomagnetic power near l = 4: 2. Temporal variation of the radial diffusion coefficient for relativistic electrons. *Journal of Geophysical Research*, *78*(22), 4600–4610. https://doi.org/10.1029/JA078i022p04600

Lanzerotti, L. J., Webb, D. C., & Arthur, C. W. (1978). Geomagnetic field fluctuations at synchronous orbit 2. Radial diffusion. *Journal of Geophysical Research*, *83*(A8), 3866–3870. https://doi.org/10.1029/JA083iA08p03866

Lejosne, S. (2019). Analytic expressions for radial diffusion. *Journal of Geophysical Research: Space Physics*, *124*, 4278–4294. https://doi.org/10.1029/2019JA026786

Lenchek, A. M., & Singer, S. F. (1962). Geomagnetically trapped protons from cosmic-ray albedo neutrons. *Journal of Geophysical Research*, *67*(4), 1263–1287.

Li, Z., Hudson, M., Paral, J., Wiltberger, M., & Turner, D. (2016). Global ULF wave analysis of radial diffusion coefficients using a global MHD model for the 17 March 2015 storm. *Journal of Geophysical Research: Space Physics*, *121*, 6196–6206. https://doi.org/10.1002/2016JA022508

Li, Z., Hudson, M., Patel, M., Wiltberger, M., Boyd, A., & Turner, D. (2017). ULF wave analysis and radial diffusion calculation using a global MHD model for the 17 March 2013 and 2015 storms. *Journal of Geophysical Research: Space Physics*, *122*, 7353–7363. https://doi.org/10.1002/2016JA023846

Li, W., Ni, B., Thorne, R., Bortnik, J., Green, J., Kletzing, C., et al. (2013). Constructing the global distribution of chorus wave intensity using measurements of electrons by the POES satellites and waves by the Van Allen Probes. *Geophysical Research Letters*, *40*, 4526–4532. https://doi.org/10.1002/grl.50920

Li, W., Thorne, R., Ma, Q., Ni, B., Bortnik, J., Baker, D., et al. (2014). Radiation belt electron acceleration by chorus waves during the 17 March 2013 storm. *Journal of Geophysical Research: Space Physics*, *119*, 4681–4693. https://doi.org/10.1002/2014JA019945

Liu, W., Tu, W., Li, X., Sarris, T., Khotyaintsev, Y., Fu, H., et al. (2016). On the calculation of electric diffusion coefficient of radiation belt electrons with in situ electric field measurements by THEMIS. *Geophysical Research Letters*, *43*, 1023–1030. https://doi.org/10.1002/2015GL067398

Lyons, L. R., & Thorne, R. M. (1973). Equilibrium structure of radiation belt electrons. *Journal of Geophysical Research*, *78*(13), 2142–2149.

Lyons, L. R., Thorne, R. M., & Kennel, C. F. (1972). Pitch-angle diffusion of radiation belt electrons within the plasmasphere. *Journal of Geophysical Research*, *77*(19), 3455–3474.

Ma, Q., Li, W., Bortnik, J., Thorne, R., Chu, X., Ozeke, L., et al. (2018). Quantitative evaluation of radial diffusion and local acceleration processes during GEM challenge events. *Journal of Geophysical Research: Space Physics*, *123*, 1938–1952. https://doi.org/10.1002/2017JA025114

Mann, I. R., Ozeke, L., Murphy, K. R., Claudepierre, S., Turner, D., Baker, D., et al. (2016). Explaining the dynamics of the ultra-relativistic third Van Allen radiation belt. *Nature Physics*, *12*(10), 978.

Millan, R., & Baker, D. (2012). Acceleration of particles to high energies in Earth's radiation belts. *Space Science Reviews*, *173*(1-4), 103–131.

Ni, B., Cao, X., Shprits, Y. Y., Summers, D., Gu, X., Fu, S., & Lou, Y. (2018). Hot plasma effects on the cyclotron-resonant pitch-angle scattering rates of radiation belt electrons due to EMIC waves. *Geophysical Research Letters*, *45*, 21–30. https://doi.org/10.1002/2017GL076028

Ni, B., Li, W., Thorne, R. M., Bortnik, J., Green, J. C., Kletzing, C. A., et al. (2014). A novel technique to construct the global distribution of whistler mode chorus wave intensity using low-altitude POES electron data. *Journal of Geophysical Research: Space Physics*, *119*, 5685–5699. https://doi.org/10.1002/2014JA019935

Ni, B., Thorne, R. M., Shprits, Y. Y., & Bortnik, J. (2008). Resonant scattering of plasma sheet electrons by whistler-mode chorus: Contribution to diffuse auroral precipitation. *Geophysical Research Letters*, *35*, L11106. https://doi.org/10.1029/2008GL034032

Olifer, L., Mann, I. R., Morley, S. K., Ozeke, L. G., & Choi, D. (2018). On the role of last closed drift shell dynamics in driving fast losses and Van Allen radiation belt extinction. *Journal of Geophysical Research: Space Physics*, *123*, 3692–3703. https://doi.org/10.1029/2018JA025190

Olifer, L., Mann, I. R., Ozeke, L. G., Rae, I. J., & Morley, S. K. (2019). On the relative strength of electric and magnetic ULF wave radial diffusion during the March 2015 geomagnetic storm. *Journal of Geophysical Research: Space Physics*, *124*, 2569–2587. https://doi.org/10.1029/2018JA026348

Omura, Y., & Zhao, Q. (2012). Nonlinear pitch angle scattering of relativistic electrons by EMIC waves in the inner magnetosphere. *Journal of Geophysical Research*, *117*, A08227. https://doi.org/10.1029/2012JA017943

Omura, Y., & Zhao, Q. (2013). Relativistic electron microbursts due to nonlinear pitch angle scattering by EMIC triggered emissions. *Journal of Geophysical Research: Space Physics*, *118*, 5008–5020. https://doi.org/10.1002/jgra.50477

Orlova, K., & Shprits, Y. (2011). On the bounce-averaging of scattering rates and the calculation of bounce period. *Physics of Plasmas*, *18*(9), 092,904.

Orlova, K., Shprits, Y., & Spasojevic, M. (2016). New global loss model of energetic and relativistic electrons based on Van Allen Probes measurements. *Journal of Geophysical Research: Space Physics*, *121*, 1308–1314. https://doi.org/10.1002/2015JA021878

Orlova, K., Spasojevic, M., & Shprits, Y. (2014). Activity-dependent global model of electron loss inside the plasmasphere. *Geophysical Research Letters*, *41*, 3744–3751. https://doi.org/10.1002/2014GL060100

Ozeke, L. G., Mann, I. R., Murphy, K. R., Jonathan Rae, I., & Milling, D. K. (2014). Analytic expressions for ULF wave radiation belt radial diffusion coefficients. *Journal of Geophysical Research: Space Physics*, *119*, 1587–1605. https://doi.org/10.1002/2013JA019204

Ozeke, L. G., Mann, I. R., Olifer, L., Dufresne, K. Y., Morley, S. K., Claudepierre, S. G., et al. (2020). Rapid outer radiation belt flux dropouts and fast acceleration during the March 2015 and 2013 storms: The role of ultra-low frequency wave transport from a dynamic outer boundary. *Journal of Geophysical Research: Space Physics*, *125*, e2019JA027179. https://doi.org/10.1029/2019JA027179

Roederer, J. G. (1970). *Dynamics of geomagnetically trapped radiation* (1st ed., Vol. 2). New York: Springer-Verlag Berlin Heidelberg.

Schulz, M., & Lanzerotti, L. J. (1974). *Particle diffusion in the radiation belts* (Vol. 7). Springer Science & Business Media.

Sheeley, B., Moldwin, M., Rassoul, H., & Anderson, R. (2001). An empirical plasmasphere and trough density model: CRRES observations. *Journal of Geophysical Research*, *106*(A11), 25,631–25,641.

Shprits, Y. Y., Drozdov, A. Y., Spasojevic, M., Kellerman, A. C., Usanova, M. E., Engebretson, M. J., et al. (2016). Wave-induced loss of ultra-relativistic electrons in the Van Allen radiation belts. *Nature Communications*, *7*, 12,883.

Shprits, Y. Y., Elkington, S. R., Meredith, N. P., & Subbotin, D. A. (2008). Review of modeling of losses and sources of relativistic electrons in the outer radiation belt I: Radial transport. *Journal of Atmospheric and Solar-Terrestrial Physics*, *70*(14), 1679–1693.

Shprits, Y. Y., Kellerman, A., Aseev, N., Drozdov, A. Y., & Michaelis, I. (2017). Multi-MeV electron loss in the heart of the radiation belts. *Geophysical Research Letters*, *44*, 1204–1209. https://doi.org/10.1002/2016GL072258

Shprits, Y. Y., Kellerman, A. C., Drozdov, A. Y., Spence, H. E., Reeves, G. D., & Baker, D. N. (2015). Combined convective and diffusive simulations: VERB-4D comparison with 17 March 2013 Van Allen Probes observations. *Geophysical Research Letters*, *42*, 9600–9608. https://doi.org/10.1002/2015GL065230

Shprits, Y. Y., & Ni, B. (2009). Dependence of the quasi-linear scattering rates on the wave normal distribution of chorus waves. *Journal of Geophysical Research*, *114*, A11205. https://doi.org/10.1029/2009JA014223

Shprits, Y. Y., Subbotin, D., Drozdov, A., Usanova, M. E., Kellerman, A., Orlova, K., et al. (2013). Unusual stable trapping of the ultrarelativistic electrons in the Van Allen radiation belts. *Nature Physics*, *9*(11), 699.

Shprits, Y. Y., Subbotin, D. A., Meredith, N. P., & Elkington, S. R. (2008). Review of modeling of losses and sources of relativistic electrons in the outer radiation belt II: Local acceleration and loss. *Journal of Atmospheric and Solar-Terrestrial Physics*, *70*(14), 1694–1713.

Shprits, Y. Y., Subbotin, D., & Ni, B. (2009). Evolution of electron fluxes in the outer radiation belt computed with the VERB code. *Journal of Geophysical Research*, *114*, A11209. https://doi.org/10.1029/2008JA013784

Shprits, Y., & Thorne, R. (2004). Time dependent radial diffusion modeling of relativistic electrons with realistic loss rates. *Geophysical Research Letters*, *31*, L08805. https://doi.org/10.1029/2004GL019591

Shprits, Y., Thorne, R., Friedel, R., Reeves, G., Fennell, J., Baker, D., & Kanekal, S. (2006). Outward radial diffusion driven by losses at magnetopause. *Journal of Geophysical Research*, *111*, A11214. https://doi.org/10.1029/2006JA011657

Spasojevic, M., Shprits, Y., & Orlova, K. (2015). Global empirical models of plasmaspheric hiss using Van Allen Probes. *Journal of Geophysical Research: Space Physics*, *120*, 10–370. https://doi.org/10.1002/2015JA021803

Su, Z., Gao, Z., Zhu, H., Li, W., Zheng, H., Wang, Y., et al. (2016). Nonstorm time dropout of radiation belt electron fluxes on 24 September 2013. *Journal of Geophysical Research: Space Physics*, *121*, 6400–6416. https://doi.org/10.1002/2016JA022546

Subbotin, D., Shprits, Y., & Ni, B. (2011). Long-term radiation belt simulation with the VERB 3-D code: Comparison with CRRES observations. *Journal of Geophysical Research*, *116*, A12210. https://doi.org/10.1029/2011JA017019

Thorne, R. M. (2010). Radiation belt dynamics: The importance of wave-particle interactions. *Geophysical Research Letters*, *37*, L22107. https://doi.org/10.1029/2010GL044990

Thorne, R. M., & Kennel, C. F. (1971). Relativistic electron precipitation during magnetic storm main phase. *Journal of Geophysical Research*, *76*(19), 4446–4453.

Thorne, R., Li, W., Ni, B., Ma, Q., Bortnik, J., Chen, L., et al. (2013). Rapid local acceleration of relativistic radiation-belt electrons by magnetospheric chorus. *Nature*, *504*(7480), 411.

Tsyganenko, N., & Sitnov, M. (2007). Magnetospheric configurations from a high-resolution data-based magnetic field model. *Journal of Geophysical Research*, *112*, A06225. https://doi.org/10.1029/2007JA012260

Tu, W., Cunningham, G., Chen, Y., Morley, S., Reeves, G., Blake, J., et al. (2014). Event-specific chorus wave and electron seed population models in DREAM3D using the Van Allen Probes. *Geophysical Research Letters*, *41*, 1359–1366. https://doi.org/10.1002/2013GL058819

Tu, W., Li, W., Albert, J., & Morley, S. (2019). Quantitative assessment of radiation belt modeling. *Journal of Geophysical Research: Space Physics*, *124*, 898–904. https://doi.org/10.1029/2018JA026414

Tu, W., Xiang, Z., & Morley, S. K. (2019). Modeling the magnetopause shadowing loss during the June 2015 dropout event. *Geophysical Research Letters*, *46*, 9388–9396. https://doi.org/10.1029/2019GL084419

Turner, D. L., Shprits, Y., Hartinger, M., & Angelopoulos, V. (2012). Explaining sudden losses of outer radiation belt electrons during geomagnetic storms. *Nature Physics*, *8*(3), 208.

Wang, C., Ma, Q., Tao, X., Zhang, Y., Teng, S., Albert, J. M., et al. (2017). Modeling radiation belt dynamics using a 3-D layer method code. *Journal of Geophysical Research: Space Physics*, *122*, 8642–8658. https://doi.org/10.1002/2017JA024143

Wang, D., & Shprits, Y. Y. (2019). On how high-latitude chorus waves tip the balance between acceleration and loss of relativistic electrons. *Geophysical Research Letters*, *46*, 7945–7954. https://doi.org/10.1029/2019GL082681

Wang, D., Shprits, Y., & Zhelavskaya, I. (2020). MLT-averaged plasmapause position calculated from the PINE plasmasphere model for the GEM challenge events.

Wang, D., Shprits, Y. Y., Zhelavskaya, I., Agapitov, O., Drozdov, A., & Aseev, N. (2019). Analytical chorus wave model derived from Van Allen Probe observations. *Journal of Geophysical Research: Space Physics*, *124*, 1063–1084. https://doi.org/10.1029/2018JA026183

Xiao, F., Yang, C., He, Z., Su, Z., Zhou, Q., He, Y., et al. (2014). Chorus acceleration of radiation belt relativistic electrons during March 2013 geomagnetic storm. *Journal of Geophysical Research: Space Physics*, *119*, 3325–3332. https://doi.org/10.1002/2014JA019822

Yu, Y., Koller, J., & Morley, S. K. (2013). Quantifying the effect of magnetopause shadowing on electron radiation belt dropouts. *Annals of Geophysics*, *31*(11), 1929–1939. https://doi.org/10.5194/angeo-31-1929-2013

Zhelavskaya, I. S., Shprits, Y. Y., & Spasojevic, M. (2017). Empirical modeling of the plasmasphere dynamics using neural networks. *Journal of Geophysical Research: Space Physics*, *122*, 11–227. https://doi.org/10.1002/2017JA024406

Zhelavskaya, I. S., Shprits, Y. Y., & Spasojevic, M. (2018). Reconstruction of plasma electron density from satellite measurements via artificial neural networks, *Machine learning techniques for space weather* (pp. 301–327). Elsevier.

Zhelavskaya, I. S., Spasojevic, M., Shprits, Y. Y., & Kurth, W. (2016). Automated determination of electron density from electric field measurements on the Van Allen Probes spacecraft. *Journal of Geophysical Research: Space Physics*, *121*, 4611–4625. https://doi.org/10.1002/2015JA022132